Chapter 1

Overview of Microwave and Optical Metamaterial Technologies

This chapter gives an exhaustive overview of the various metal and dielectric artificial material technologies that are currently developed in the microwave and optical regimes. Starting from the first proposals for negative index materials (NIMs), based on a split-ring resonator (SRR)/wire scheme, we show how this basic pattern has progressed to solving the problem of normal incidence with the so-called fishnet structure and to broadband with a transmission line approach. Full dielectric metamaterials whose operation relies on Mie resonance in the long wavelength regime or on band folding, close to the Bragg conditions, complete this analysis.

1.1. Introduction and background

Electromagnetic (EM) metamaterials are now attracting much interest owing to their singular properties notably with the achievement of *negative* effective parameters [CAI 09, SOL 09, RAM 08, MAR 08, ELE 05]. For illustration, Figure 1.1 shows the possibilities afforded by these engineered artificial materials by plotting the effective permeability (real part μ_r) versus effective permittivity (real part ε_r) diagram. With respect to *conventional* natural or structured materials with *positive* index value $n = (\varepsilon_r\mu_r)^{1/2}$, with extreme values (notably relative permittivity and permeability ε_r, $\mu_r > 100$

Chapter written by Didier LIPPENS.

through the use of ferroelectrics and ferromagnetics materials), metamaterials allow the fabrication of: (1) epsilon negative (ENG materials: $\varepsilon_r < 0$ and $\mu_r > 0$) or near-zero (NRZ) permittivity material (NRZ materials: $\varepsilon_r \sim 0$), (2) mu negative (MNG materials with $\mu_r < 0$ and $\varepsilon_r > 0$) and (3) double negative media (DNG with $\mu_r < 0$ and $\varepsilon_r < 0$).

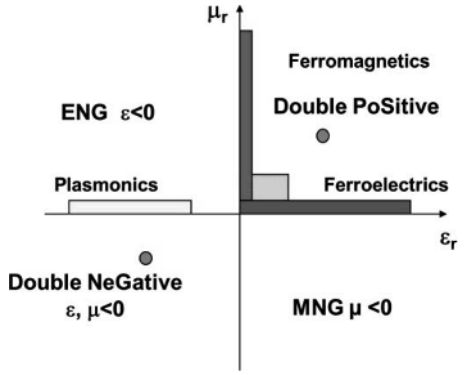

Figure 1.1. *Effective parameter space: ferroelectric and ferromagnetic natural materials enable the fabrication of extreme permittivity (ε_r between 100 and 1,000 for Barium Strontium Titanate material for instance). Metallic compounds involved in the fabrication of plasmonics devices such as gold or silver layers exhibit a naturally negative dielectric constant below their plasma frequency. As a result, they can be considered as ENG materials. Their structuring designs their dispersion characteristics via the plasma frequency engineering. MNG materials involve current loops*

From the viewpoint of EM wave propagation, metamaterials give the possibility of accurately controlling the following:

– The *phase* of the reflected waves in mirror-like devices (out-of-phase for a perfect electrical conductor (PEC) and in phase for a perfect magnetic conductor (PMC), also called artificial magnetic conductor (AMC)).

– The *backward* propagation for NIM (equivalent to DNG materials), which means that the group and phase velocities are antiparallel.

– The $\boldsymbol{k}$ vector magnitude including quasi-infinite wavelength for near-zero permittivity or balanced composite right–left-handed metamaterials (CRLH).

– The *negative* refraction angle (same half-space with respect to the impinging wave).

– The focusing of a point source placed in front of a NIM flat lens. Also *super-resolution* below the *Rayleigh diffraction limit* can be considered on the basis of the so-called amplification of evanescent waves.

In a first approximation (by neglecting the dispersion of constitutive materials), the EM characteristics scale to the size of the basic cell, whose relevant dimensions have to be much shorter than the operating wavelength to satisfy homogeneity conditions. From this scaling rule, it results that device operation over an *ultra-broad frequency band* (from radio frequency to visible optics) can be envisaged by downscaling all the relevant dimensions [RAM 08, SOL 09, CAI 09].

Basically, artificial media involve a structural transformation at the origin of the negative values of their effective constitutive parameters. This concept can be understood simply from the recognition that the response of a material to an impinging wave is *out-of-phase* with respect to the excitation, provided that the driving signal frequency is above the characteristic resonant frequency of the system. This basic principle is true (1) for cut-wire arrays, which exhibit a Lorentz-type permittivity dispersion (Figure 1.2), (2) for negative permeability plasmonic resonators and (3) for Mie resonance-based dielectric resonators.

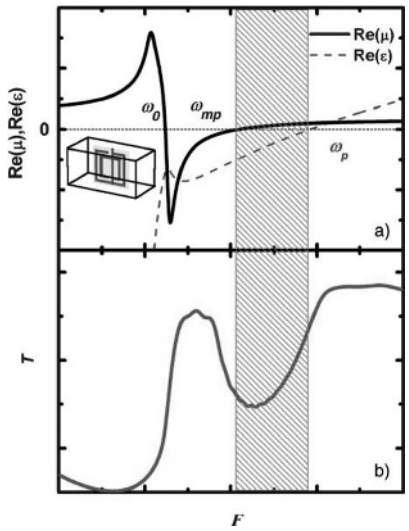

Figure 1.2. *Dispersion characteristics of constitutive parameters. MNG are fabricated from artificial structures mainly involving metallic current loops as in a miniaturized solenoid. DNG are achieved via the combination of ENG and MNG media. Propagation characteristics can be predicted on the basis of the dispersion of the effective (apparent) permittivity and permeability. Generally, μ_{eff} obeys a Lorentz-type (resonant) frequency variation while ε_{eff} follows a Drude-type (non-resonant) frequency dependence*

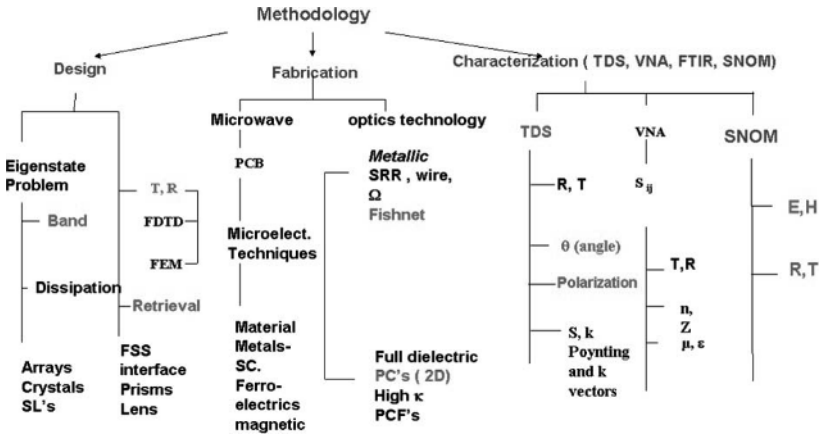

Figure 1.3. *Illustration of the methodology for the realization of artificial materials including the design, the fabrication and the experimental assessment. In grey character: the key issues addressed in this review*

A general study methodology is summarized in Figure 1.3. It consists of three stages permitting us to (1) first predict the geometrical specifications according to the data of the material constituents, (2) to synthesize the artificial structures and (3) to experimentally verify the targeted propagation characteristic resulting from the scattering of light with these artificial media. With respect to the design stage, the first step concerns solving the eigenstate master equations. With the target to achieve a highly dispersive EM characteristic, a large number of metamaterial structures are intrinsically resonant. Also, most of the microstructures used in metamaterial fabrication are periodic arrays. This periodicity condition is not strictly necessary since the basic response is due to the scattering of impinging waves on an isolated cell. However, it is worth mentioning that the coupling effects between basic cells, in densely packed arrays, play an increasing role, notably in the case of symmetry breaking that gives further degrees of freedom in the functionality of the devices. For instance, it was just shown that the *coupling* between an SRR (often considered as the canonical meta-atom) and its mirrored image by a PEC permits us to adjust the resonant frequency over a 10% fractional bandwidth. The counterpart of the highly dispersive nature of metamaterials is the *loss* issue and the second major stage in the device design is the estimate of the intrinsic and extrinsic loss contributions. The latter is of prime importance for the necessary impedance matching of a metamaterial to its environment. On this basis, the scattering parameter characteristics or,

equivalently, the complex transmission and reflection coefficients can be derived by using home-made or commercially available simulation codes.

With respect to the fabrication technologies, we have to distinguish between those enabling the fabrication of microwave devices and those that are employed for the fabrication of structures operating in the optical spectrum.

For the former, conventional printed circuit board (PCB) technology can be used for the host substrate and the metal patterns such as strips, pads, gaps, slots or apertures. These patterns generally form the basic cell of the metamaterial-inspired structure. However, in many cases, some originality can be drawn from the fact that structuring is realized on a micro- or nanometer scale with, thus, a very high aspect ratio between the wavelength and the relevant dimension of the basic cell.

In connection with the optics technology [LIU 08, JOA 08, KAN 11], two classes of device will be considered, namely plasmonic devices (in this case, metals are used as free-standing structures or deposited onto host dielectric substrates, including multilayered structures with dielectric spacing) or full dielectric micro- and nanostructures. The latter includes *photonic crystal*s, paying attention to their unusual dispersion characteristic rather than to their band gap. These dielectric structures are generally made up of semiconductors for their compatibility to integrated optics. Specially, this means the possibility of fabricating, for instance, hole and pillar arrays that exhibit negative refraction when operating in the second band of the dispersion diagram, or fabricating the so-called gradient index lens by varying the relevant dimensions of the basic cell locally.

At last with respect to the characterization stage, various techniques will be employed including first vector network analysis that is mainly dedicated to the analysis of microwave and millimeter wave metamaterials. The main advantage of this technique is the record of the magnitude and phase of the reflection (R) and transmission (T) characteristics that allow the *effective parameters* to be retrieved without any ambiguity [SMI 02]. Also, the mapping of the EM fields brings information of prime importance for the verification of wave bending via gradient index structures such as those involved in focusing and cloaking devices.

Turning now to the terahertz frequency range, in practice between 0.3 and 3 THz, the most powerful technique is the time domain spectroscopy (TDS) that also gives access to the magnitude and phase of R and T. These techniques can be used in a complementary manner by considering first the

frequency assessment of the dispersion of constitutive materials and then the characterization, at the device level, after microstructuring.

For the optics side, the experimental verification can be based on scanning near-field optical microscopy (*SNOM*) and Fourier transform infrared (*FTIR*). Basically, these techniques only provide magnitude information. However, an additional set-up can be used in order to get access to the phase data. A differential measurement, as is performed in TDS experiments, seems to be one of the most promising tracks toward this possibility of measuring simultaneously phase and magnitude.

At microwaves, the generic structure is made up of *SRRs* and *wire* arrays [PEN 96, PEN 99]. In this chapter, it will be shown that omega-type patterns are equivalent to a double negative medium (with a left-handed dispersion branch) in a relatively broad frequency range, which can be balanced with a right-handed dispersion branch. This EM artificial structure called CRLH metamaterial can be used for a beam steering wedge-type device such as the one discussed in the next section.

In a second part, we show how a full dielectric approach can replace the metal (plasmonic) approach by mainly targeting the isotropy of EM characteristics. This technology, known as a Mie resonance-type approach [MIE 08, LEW 47] will be exemplified via ferroelectric cube arrays. For both approaches (plasmonic and full dielectric), we show how tunable EM characteristics can be achieved by modifying the resonant frequency notably with the infiltration of liquid crystal (LC) whose orientation is controlled. In addition, it can be shown that backward waves, corresponding to a negative index, can be achieved by periodically loading a transmission line by series capacitances and shunt inductances. This *transmission line* approach will be briefly addressed in this chapter with the main emphasis on bulk structures. However, the transmission line approach is further developed by Bruno Sauviac in Chapter 2.

1.2. Omega-type arrays

Figure 1.4 illustrates the omega-type technology [HUA 04, LHE 07, SIM 03, ZHA 08a], with a schematic of the basic cell (a) along with the stacking scheme (b). The interconnected arms of the omega motifs constitute a *continuous* wire array (Drude-like dispersion) at the origin of the electrical activity. The C-shaped core is equivalent to the so-called SRR [PEN 99] that gives rise to a magnetic activity with a Lorentz-type dispersion characteristic.

Indeed, for a proper polarization of the magnetic field, i.e. normal to the metallic pattern (grazing incidence), the induced current in the metal loop yields a magnetic response (B) that is out-of-phase with respect to excitation field H. From the constitutive equation $B = \mu H$, it can be noted that the effective permeability is negative. From Figure 1.4, it can be seen that the basic cell consists of two omega patterns with a back-to-back configuration, aiming at cancelling the current induced by the electrical stimulus (through the gap) in the metal loop. It can be shown that such an arrangement is equivalent to broadside coupled SRRs [MAR 08].

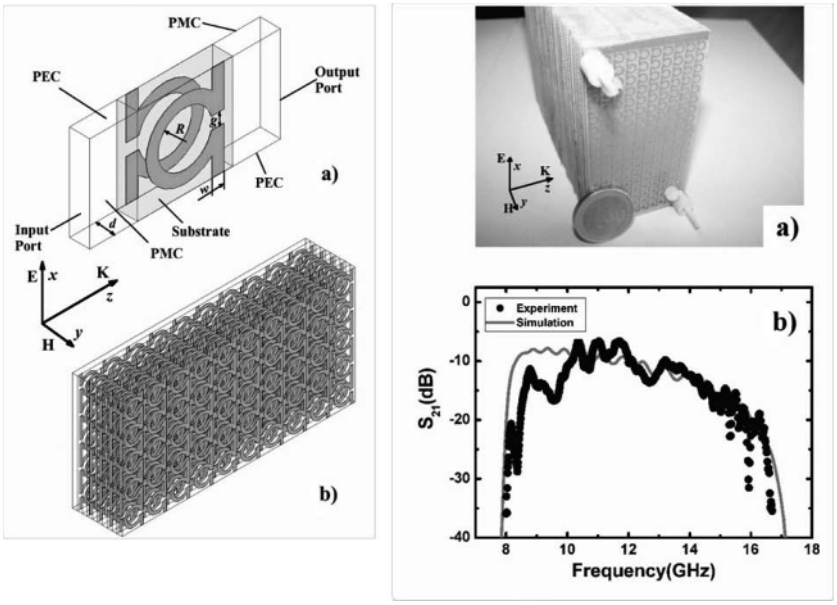

Figure 1.4. *Illustration of a balanced composite right–left-handed (CRLH) bulk metamaterial fabricated from omega-type motifs. Left panel a) basic cell and b) 3D configuration of the layered structure (the wire array corresponding to the omega arms is continuous for a Drude-like dispersion characteristic). Right panel a) image of a prototype operating in X- and Ku-bands and b) frequency dependence of the transmission coefficient S_{21}*

1.2.1. *Dispersion and angular properties*

In this chapter, the geometrical dimensions are chosen for an operation at centimeter wavelengths, with relevant dimensions (strip metal width (w), slot (g) and ring radius (R) typically one order of magnitude smaller than the

operating wavelength in order to satisfy the metamaterial regime (see section 1.1). In practice, this means dimensions on a millimeter scale.

Figure 1.4 shows the transmission characteristic (modulus of the scattering parameter S_{21}) of a slab-type prototype, fabricated by using PCB technology (image in inset). S_{21} was measured by means of a vector network analyzer (VNA) and the frequency response is compared with the results of full wave simulations. From this figure, it can be seen that the device exhibits a broadband transmission window between 8 and 16 GHz. This broadband is a result of a *balance CRLH* dispersion characteristic as aforementioned. This means that the transition between the left-handed (negative index) and the right-handed dispersion branches is seamless (no forbidden gap between them). At the turning frequency, the refractive index is zero with a non-vanishing group velocity ($v_g = \partial\omega/\partial k$). At this stage, it should be emphasized that this situation is totally different from a near-zero index via a zero permittivity value since *both* the effective permittivity and permeability are null at the same frequency. In terms of dispersion characteristic, this means that the electrical plasma frequency (ω_{pe}) equals the magnetic plasma frequency (ω_{pm}). The simulations carried out for assessing the transmission properties of a slab-type device were conducted by creating the periodicity via appropriate boundary conditions. The direct description of the whole structure under test can thus be simulated. However, it is clear that this *ab initio* approach is time consuming and very demanding in computational resources. As a result, it seems suitable to examine whether the metamaterial structure can be described via its effective parameters (ε_{reff} and μ_{reff}). There is a plethora of literature that addresses the equivalence between the EM response given by an effective medium approximation and the real geometrical configuration. We show hereafter that such an approximation is valid for the omega structures, provided that permittivity and permeability tensors are used for the constitutive equations (see Table 1.1).

Details for the retrieval of dispersion characteristics can be found in references [SMI 02, CRO 08b]. On the basis of this tensor approach, the direction of the refracted beam can be predicted numerically under a homogeneous medium approximation and compared with the exact solution taking all the details of the microstructure into account. This comparison is carried out for two representative frequencies corresponding to negative and zero values of the effective index represented by the field maps of Figure 1.5.

Frequency		10.9	12.8	15.0
n		–1.0052	–0.038	0.777
ε	ε_x	–3.49 + 0.13i	–0.17 + 0.04i	4.90 + 0.57i
	(tan ε_x)	(–0.036)	(–0.234)	(0.117)
	ε_y	4.07 + 0.08i	4.07 + 0.08i	4.07 + 0.08i
	(tan ε_y)	(0.02)	(0.02)	(0.02)
	ε_z	15.56 + 0.36i	16.66 + 0.38i	15.74 + 0.24i
	(tan ε_z)	(0.023)	(0.02)	(0.0153)
μ	μ_x	0.99 + 0.00034i	0.9858 + 0.0003i	0.9850 + 0.0003i
	(tan μ_x)	(0.0003)	(0.0003)	(0.0003)
	μ_y	–0.28 + 0.03i	0.0082 + 0.0002i	0.1232 + 0.005i
	(tan μ_y)	(–0.091)	(–0.022)	(0.04)
	μ_z	1.050 + 0.007i	1.055 + 0.002i	0.818 + 0.002i
	(tan μ_z)	(0.007)	(0.002)	(0.002)
θ_r (°) (Retrieval value)		–30.6°	–1.10°	23.2°
θ_r (°) Homogeneous prism		–28.6°	–2.6°	21.5°
θ_r (°) Microstructured prism		–25.6°	–0.4°	25.4°

Table 1.1. *Permittivity and permeability tensors for three relevant frequencies of an omega-type metamaterial operating at microwaves (negative, null, and positive index frequencies). Comparison is made in terms of the refracted angle for a wedge-type device by assuming anisotropic and isotropic values of the constitutive parameters and determined from full wave analysis (microstructured prism)*

From this figure, it can be noted that similar behavior is predicted for the homogeneous and the microstructure approaches in the near field via the mapping of the electric field magnitude and, in the far field, through the plot of the radiation patterns. By changing the operating frequency, negative, zero and positive refraction angles can be achieved continuously in the vicinity (near-field condition) of the tilted interface of this wedge-type device. As a result in the far field, the radiation pattern is steered around the normal to the wedge interface.

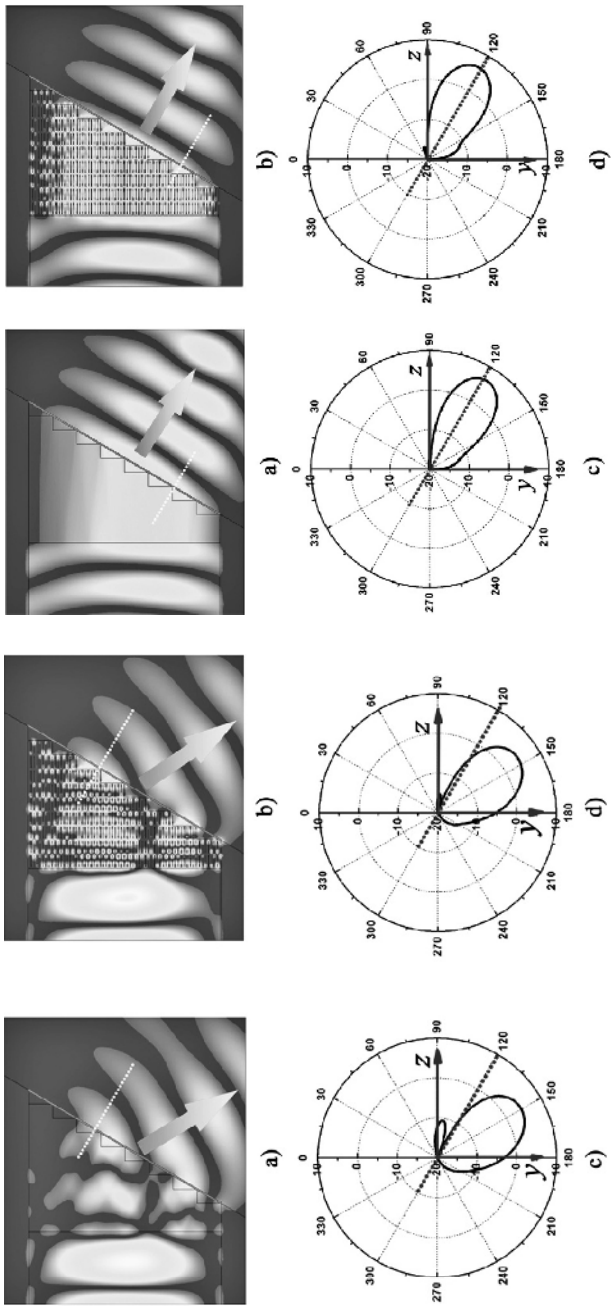

Figure 1.5. *Comparison between the near field response of a prism-like device made up of omega-type arrays and approximated by using the effective medium theory for f = 12.8 GHz (above side) and 10.9 GHz (below side)*

Experimental verification of the aforementioned beam steering can be demonstrated by using a scattering chamber such as the metal dual plate. For clarity, the top metal plate was removed in Figure 1.6(a) showing an image of the experimental set-up. The EM waves are radiated and detected via rectangular horn antennas connected to a VNA. In addition, absorbing materials slabs are positioned on the sides of the input path (between the input horn and the sample under test). In Figures 1.6(c) and (b), the angle dependence along with the image of a prism-like device are displayed, respectively. This structure has also been fabricated by means of stacked PCBs. According to the operation frequency *(f)*, it can be shown that the maximum of the detected signal peaks around $\theta = -22°$ for f=12 GHz, $\theta = 0°$ for 13.6 GHz and $\theta = +13°$ for f = 15 GHz.

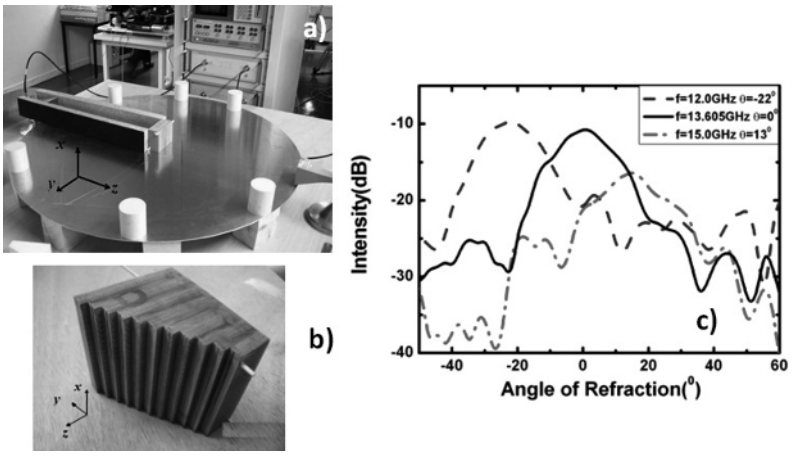

Figure 1.6. *a) Image of a scattering chamber using a parallel plate set-up (for clarity, the upper metal plate was removed), b) image of a wedge-type device and c) angle dependence of the refracted beam for three operating frequencies*

1.2.2. *Tunable omega-type structure*

The previous example shows the possibility of tuning the EM properties via a change of the operating frequency. However, in many practical applications, it is interesting to vary the operating point at a fixed frequency. This can be done by changing the dielectric properties of the constituent materials. In the following, such a change is exemplified via the use of LC technology [ZHA 08c, ZHA 08d].

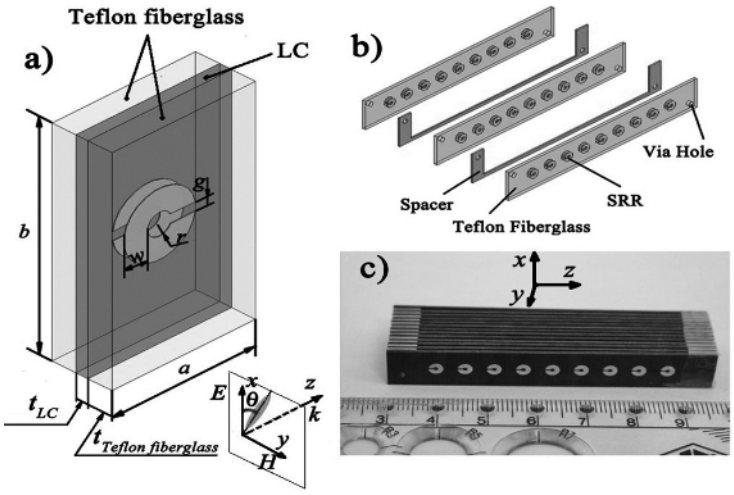

Figure 1.7. *Experimental demonstration of the tunability of single negative media (broadside coupled SRR-type motif). Tunability is achieved via liquid crystal (LC) infiltrated between the SRR-patterned array. Ellipsoidal-shaped nematics are reorientated by means of permanent magnets (not shown here)*

Indeed, it is well known that LCs such as nematic compounds are birefringent. This means that they exhibit different index values along the long and short axes of the ellipsoidal-shaped molecule (see inset of Figure 1.7 for illustration). The LC molecules can be oriented primarily, for instance via interface states, but also *reoriented* by means of external stimuli such as magnetic or electric fields. The underlying idea for tuning the properties of metamaterials is to reorientate LC films that are infiltrated within the two back-to-back C-shaped motifs of omega particles [ZHA 08a]. For the sake of clarity, a single negative medium, with negative value of the effective permeability while the effective permittivity is positive, is considered as an intermediate stage. The basic cell of the magnetic negative (MNG) medium is shown in Figure 1.7. The fact of using a back-to-back gap configuration is motivated by the search for a pure magnetic response as briefly explained earlier, by cancelling the electric field induced currents. Under the condition of a single negative medium, the index is purely imaginary. In terms of propagation properties, this corresponds to evanescent waves in the frequency band where μ_{reff} is negative. As a result, we expect a stop band rather than a passband transmission characteristic. For tunability purposes, according to the aforementioned basic principle, LCs are infiltrated between the two metal C-shaped motifs by means of spacer layers as illustrated in Figure 1.7. Their

reorientation (θ angle) as a function of the electric field polarization is controlled experimentally via permanent magnets. An image of a prototype is shown in Figure 1.7 [ZHA 09a].

In Figure 1.8, the frequency dependence of the transmission coefficient, measured through VNA and calculated by full wave analysis, is compared. Similar trends are obtained for calculated and measured data in agreement with the frequency shift predicted when θ is increased step by step between 0° and 90°.

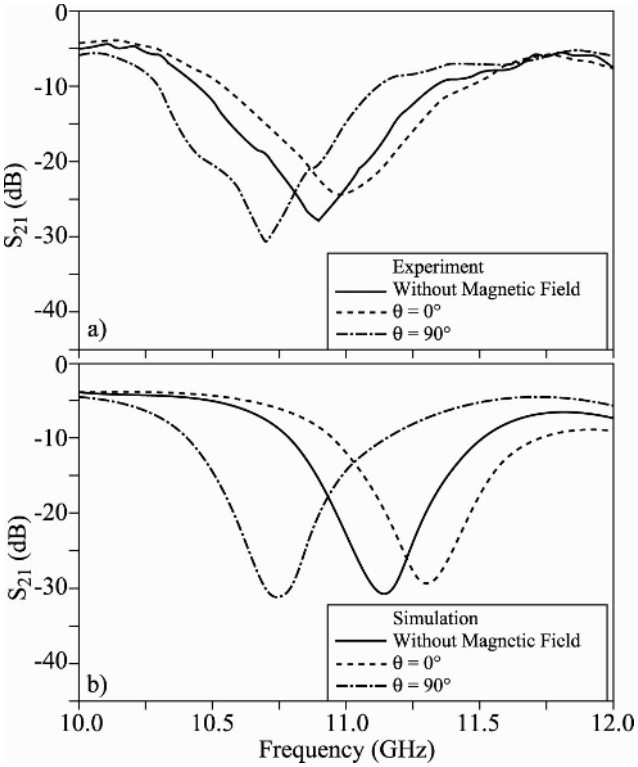

Figure 1.8. *Comparison between the frequency dependence of the S_{21} scattering parameter (experiment a) and simulation b)) for single negative permeability metamaterial. A stop band response is achieved with the possibility of tuning the anti-resonance dip by the reorientation of the infiltrated nematic molecules*

For a comprehensive study of the capabilities of the omega-type structures, we will now consider their operation at millimeter wavelengths.

1.2.3. *Omega-type pattern at millimeter wavelengths*

SRR/wire arrays [GOK 06, CRO 08a] and omega-type patterns [ZHA 08e] can also be used at higher frequencies at the cost of challenging technologies to satisfy the reduction in dimension. Therefore, instead of using PCB technology, monolithic integration has to be involved for stacking the various metal layers (Figure 1.9).

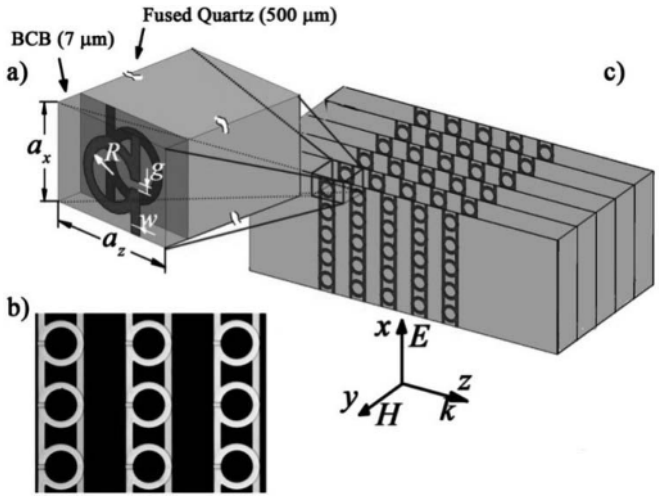

Figure 1.9. *Illustration of the monolithic stacking techniques for bulk metamaterial operation at millimeter wavelengths; a–c) schematic of the stacked arrangement of arrayed omega-type pattern with a close up view of the basic cell along with an image of the broadside coupled omega chains*

The FR4 dielectric substrates have been replaced by 7-µm-thick benzocyclobutene (BCB) layers deposited on fused silica substrates. As an example of the possibilities afforded by monolithic fabrication techniques, Figure 1.10 illustrates the transmission characteristic of an omega-type prototype aimed at operating at millimeter wavelengths.

Unlike the previous prototype operating at centimeter wavelengths, in the present case, there exists a band gap between the left- and right-handed dispersion branches. This can be noted in the frequency dependence of the magnitude S_{21} around 90 GHz. For identifying the left- and right-handed character of the passbands lying between 75 and 95 GHz and 100 and 110 GHz, respectively, we also plotted the phase of S_{21} for two prototypes of

different length, namely including 10 and 14 cells. We can note a positive phase difference for the former band while the difference becomes negative for the high-frequency band. This property is the signature of a cross-over within the gap. Also shown in the variation of the magnitude of S_{21} is the retrieved refractive index by a Fresnel inversion method [CRO 08b]. The value of the real part of n_{eff} is negative in the lower part of the W-band (50–75 GHz) corresponding to a backward wave and positive above 100 GHz. In the forbidden gap, the real part of n_{eff} is zero.

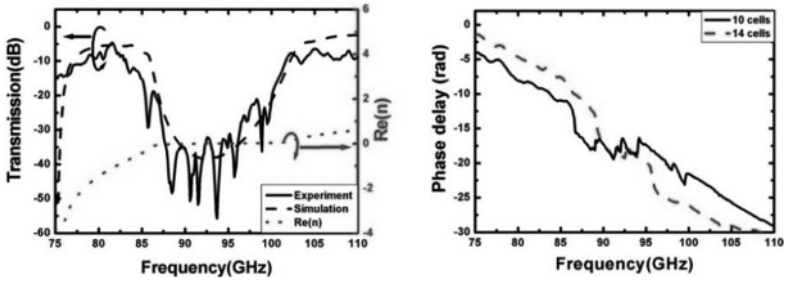

Figure 1.10. *Measured (solid line) and calculated (dashed line) transmission spectra, along with the retrieved effective index (dotted lines) versus frequency. Direct experimental evidence of the reversal of the k vector with respect to the Poynting vector, with a phase advance between 75 and 85 GHz and a phase delay between 85 and 110 GHz*

1.2.4. *SRRs at infrared*

The SRR technologies can also be extended to a higher frequency and notably in the infrared spectrum. The general concept, namely the phenomenon of a current loop, is scalable in frequency. As a result, negative values of the effective permeability can be expected up to the cutoff frequency of the material constituents, which corresponds to the plasma frequency for the metal layers. However, it is important to note that increasing the operating frequency up to visible optics is problematic due to the contribution of the kinetic inductance. This phenomenon will be detailed by Philippe Tassin in Chapter 8.

Not taking into account this physical effect, designing a SRR-based metamaterial for the infrared domain already faces several difficulties. The major difficulty arises from the requirement of an H-field excitation normal to the current loop plane. The other difficulty is the challenging fabrication technique of relatively large area samples, generally on the centimeter scale for proper illumination of the impinging wave, while the dimension of the

basic cell is reduced dramatically. As a result, it is generally thought to simplify the pattern of the basic cell by only keeping the key feature. The C-shaped structure satisfies this condition and most of the studies reported in the literature are based on such a simplified pattern [LIN 04, SOU 07]. For illustration [LIP 09], a scanning electron micrograph of a C-pattern array designed for operating at mid-infrared (typical wavelengths of 10 μm) is shown in Figure 1.11. The dimension is apparent in this figure and all the relevant dimensions, notably the periodicity, are less than 1 μm. The metamaterial criterion, i.e. the fact that all the dimensions are far shorter than the operating wavelength, is met by means of electron beam lithography. The device was characterized by FTIR spectroscopy while the frequency responses of the scattering parameters were calculated with the help of full wave codes. Figure 1.12(b) compares numerical results (upper panel) to the measured results for the two values of the electric field orientation along the gap-bearing arm (solid line) and for the E-field polarized normally to this direction (dotted lines). Calculation and experiment agree well with a pronounced dip on the transmission around 30 and 100 THz for an E-field polarization parallel to the gap-bearing arm and around 75 THz for the perpendicular polarization. From the retrieval procedure, using Fresnel inversion techniques, it can be shown that the electric response dominates the scattering of the impinging wave. Indeed, the experiment was conducted *under normal incidence* and hence with the magnetic field direction parallel and not perpendicular to the SRR plane. Strictly speaking, there is no pure magnetic activity in the present case because the magnetic moment is generated by a current loop induced by the EM force across the gap.

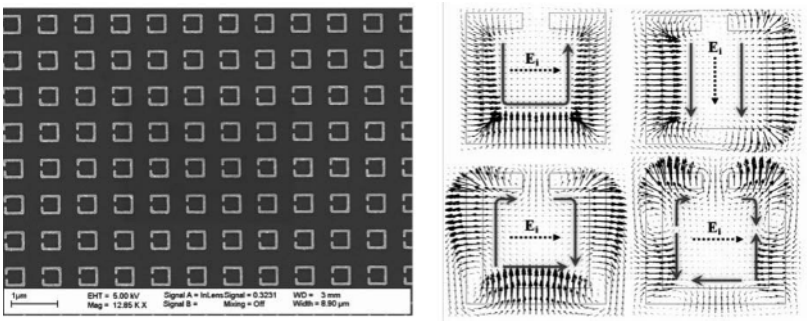

Figure 1.11. *Scanning electron microphotograph (SEM) of a split-ring resonator array for a mid-infrared operation and field mapping illustrating the various resonance modes for two polarization directions of the impinging EM field along and transverse to the gap-bearing arm*

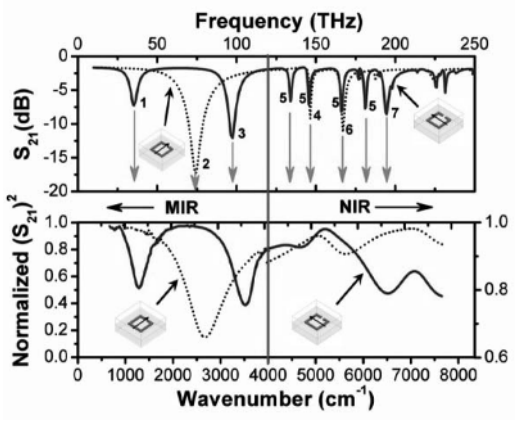

Figure 1.12. *Comparison of the transmission spectra calculated by finite element modeling (High Frequency Structure Simulator code (HFSS™)) and measured by means of FTIR experiments (respectively, solid line and dotted line)*

How to preserve a current loop induced by the incident magnetic field and not the electric field for observing a pure magnetic response will be addressed in the following with the introduction of the so-called *fishnet structure*. Before this, we will show how to broaden the left-handed dispersion branch using a *transmission line approach*. This will be performed by means of two representative prototypes operating at centimeter and millimeter wavelengths, respectively. This will permit us to illustrate the vector network analysis and the TDS characterization techniques.

1.3. Transmission lines with series capacitances and shunt inductances

The basic idea for achieving negative values of the effective index in a transmission line model was first proposed in the following references [OLI 02, CAL 04, CAL 06]. Unlike conventional transmission lines that are described by means of distributed series inductance L_{RH} and shunt capacitance C_{RH} (lossless case), RH standing for right handed, the circuit also consists of series capacitance C_{LH} and shunt Inductance L_{LH}. The result of a dual configuration on the propagation properties is a phase advance giving rise to backward propagation. This property was already reported in the literature several decades ago. The underlying idea is to combine both right- and left-handed features in order to achieve a *balanced CRLH* dispersion characteristic that was already pointed out in the analysis of the omega-type array in the previous section.

1.3.1. *Tuneable phase shifter for centimeter wavelengths*

As an illustration of the CRLH properties, we will present the key results of the study reported in [MAR 09] that makes use of a coplanar wave guide technology (see Figure 1.13).

The series capacitance C_{LH} is designed by means of an interdigited pattern. The shunt inductances are realized with stub-like motifs. In this section, a thin ferroelectric film is deposited onto the substrate prior to the metallization for tunability purposes [VEL 06]. The inductance metal strips are also used for biasing the electronically controlled capacitance through the variation of the permittivity of ferroelectrics films. However, bounded shunt wires ensure the electric continuity of the lateral ground planes.

The measured dispersion characteristics, which can be retrieved from the complex scattering parameters measurements performed in X and Ku bands, are shown Figure 1.13(b). It can be shown that the transition between the left-handed dispersion branch (negative value of k with a corresponding positive group velocity) and the right-handed dispersion branch is seamless and thus without any forbidden gap between the two transmission bands. From the inset of Figure 1.13, it can be shown that biasing the varactors allows shifting positively the corner frequency between left- and right-handed bands.

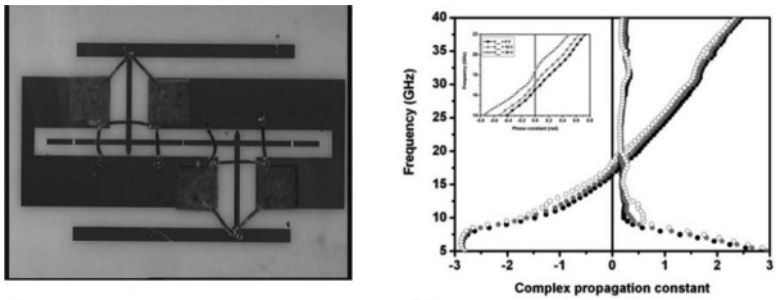

Figure 1.13. *Image of a prototype based on a CPW transmission line loaded with series capacitances and shunt inductances. Voltage controlled capacitances are integrated here by means of a ferroelectric (BST) thin film. Dispersion characteristics for various DC voltages controlling the ferroelectric film permittivity*

1.3.2. *Left-handed transmission lines at tetrahertz frequencies*

The transmission line approach is not restricted to the centimeter wavelengths. Here again, the extension toward higher frequencies is

challenging in terms of fabrication techniques and experimental assessment. Indeed, it is shown that most of the metamaterial effects are related to the control of the dispersion and hence of the phase of the propagating waves. This involves accurately controlling not only the magnitude of the transmitted wave, by avoiding as far as possible any loss contribution, but also the phase through the artificial structure. Although the scattering parameters measurement via VNA allows the determination of the complex elements (magnitude and phase) of the scattering matrix [S_{ij}], it is imperative to preserve this measurement of the phase at millimeter and sub-millimeter wavelengths. For commenting such an issue, the key results of reference [CRÉ 05] are reproduced here and discussed via the illustrations shown in Figure 1.14. The upper panel shows a scanning electron microphotograph of a dual strip transmission line loaded by series capacitances and shunt inductances. The series capacitances were realized by means of a metal overlay deposited onto a dielectric layer (Si_3N_4). The series inductances are designed by folded narrow strip patterns using electron beam lithography while plasma reactive etching was used for defining the capacitances locally.

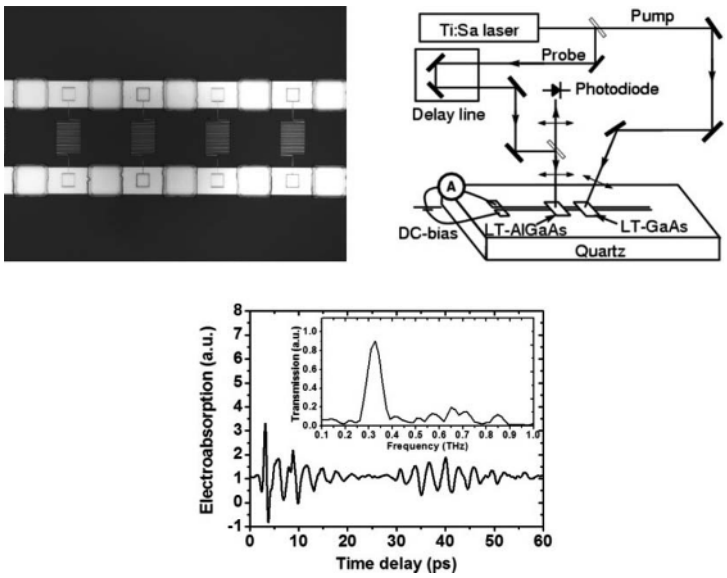

Figure 1.14. *Scanning electron microphotograph of a left-handed coplanar strip transmission line operating around 0.3 THz (far infrared spectral region) with parallel plate series capacitance and meander-like shunt inductances. Schematic of the pump-probe time domain spectroscopy (TDS) using low temperature (LT) grown GaAs-based semiconductor patches. Time and spectral response showing a transmission window at the millimeter/sub-millimeter wavelength transition. Propagation is backward*

The right panel of Figure 1.14 shows a schematic of the experimental set-up with a voltage pulse generated across the two strips of the transmission line by a femtosecond laser illumination. To preserve the phase information, a pump probe scheme was used. In short, the laser pulse supplied by a femtosecond Ti/Sa laser (typical pulse duration of about 100 fs) is split into two beams. The pump optical beam creates a voltage pulse owing to the shunt of the two transmission lines strip by photoionization. The probe beam allows the tracking of the transmitted signal via a photodiode that converts the electrical pulse into an optical one. The detection of the transmitted pulse in magnitude and phase is achieved through the phase coherency of the two laser beams. The TDS used in this chapter is a sampling technique that allows the recording of the transmitted wave versus time. Subsequent Fourier transform allows the reconstruction of the passband with subsequent analysis through Fresnel inversion. The bottom panel of Figure 1.14 shows the time and frequency response of a typical device designed for operation at the transition between the millimeter and the sub-millimeter wavelengths (300 GHz). Direct evidence of the left-handed character can be achieved by tracking in real time the phase advance of the transmitted wave in the left-handed dispersion branch. Another clue of the left-handed character can be obtained by comparing the phase shift between two lines with a different number of cells in a manner similar to the one described for omega structures operating around 100 GHz (see section 1.2.3).

To our knowledge, the aforementioned study is among the highest frequency experimental evidence of backward propagation. For an extension into the far infrared and targeting an operation at mid- and near infrared, it is imperative to select another configuration that is called fishnet. This is addressed in the following section.

1.4. Fishnet approach

Turning now to the so-called fishnet approach that was first introduced in optics, Figure 1.15 shows the key illustration of the study reported in [ZHA 11]. It is important to note that the basic cell, displayed in the left-hand panel, is primarily made up of a tri-layered structure that consists of a dielectric slab sandwiched between two metal films. Such a configuration is motivated by the search for inducing a current loop by the incident magnetic field and not the electrical one *under normal incidence*. Indeed by coupling two metal planes via the displacement current within the dielectric spacer, it can be shown that a current loop is formed provided that the conduction currents in the metal layers are antiparallel. However, wire arrays can be responsible for the creation of an electrical dipole as in conventional

wire/SRR arrays. As a result, for a proper determination of the dimensions, it is now possible to fabricate a double negative medium (negative index material) for excitation under normal incidence.

1.4.1. *Tunable fishnet for centimeter wavelengths*

In this section, the realization of a tunable fishnet metamaterial operating at centimeter wavelengths is illustrated on the basis of the work reported in [ZHA 11]. Figures 1.15(a) and (b) show schematic views of a tunable fishnet metamaterial structure, which is composed of three layers, i.e. a pair of fishnet topologies patterned on the surface of Teflon fiberglass slabs with void in between designed to be infiltrated with a nematic LC. The underlying idea for tuning the LH passband is to change the effective permittivity of substrate via LC molecular reorientation, by applying a DC voltage between the top and bottom metal layers. To achieve all angle LC reorientation between 0° and 90° and hence a large tuning range, a thin layer of polyimide (PI) was spanned on the surface of Teflon substrate and copper element to force nematic LC to align parallel to the metal surface. As a combination of electrical dipoles and current loops, providing simultaneously negative permittivity and permeability, a fishnet structure can operate under normal incidence. The frequency dependence of the transmission, measured under various bias voltages has been compared with full wave calculations (Figure 1.16). As shown in this figure, for the initial alignment with the LC director parallel to the fishnet surface, there is a well resolved peak with a relatively high intensity transmission peak around 9.01 GHz, which is separated from a quasi-unit transmission shoulder, starting from 11.0 GHz, by a shallow dip. As the LC director is orientated from 0º to 90º, it is shown that the ground transmission peak is shifted downward 8.60 GHz, accounting for 400 MHz frequency variation, whereas the second passband is nearly unchanged.

1.4.2. *Terahertz subwavelength holes arrays*

Primarily, subwavelength hole arrays were introduced for the observation of the so-called extraordinary transmission defined in the literature by the acronym EOT [EBB 98]. The term “extraordinary transmission” characterizes the fact that the transmission through a screen perforated by subwavelength apertures may exceed the ratio between the surface of the holes and the whole illuminated area. It is now well-established that the transmission through a hole in a metal plate exhibits a cutoff frequency that is related, in a first approximation, to the condition that the whole diameter fits half the wavelength. This cutoff was predicted theoretically by Bethe. Under the EOT

condition, it can be shown that a device made of a single hole or of a hole array enhances transmission levels with respect to the values predicted by direct geometrical considerations. As a result, much higher transmittance values than those predicted in the framework of the Bethe diffraction theory are achieved. This enhancement in transmissivity is observed at specific frequencies involving complex transmission mechanisms. Notably, surface waves called surface plasmon polaritons are evidenced in optics (spoofs plasmon waves at terahertz) between the upper and lower interfaces, between the metal and its background medium (air for instance).

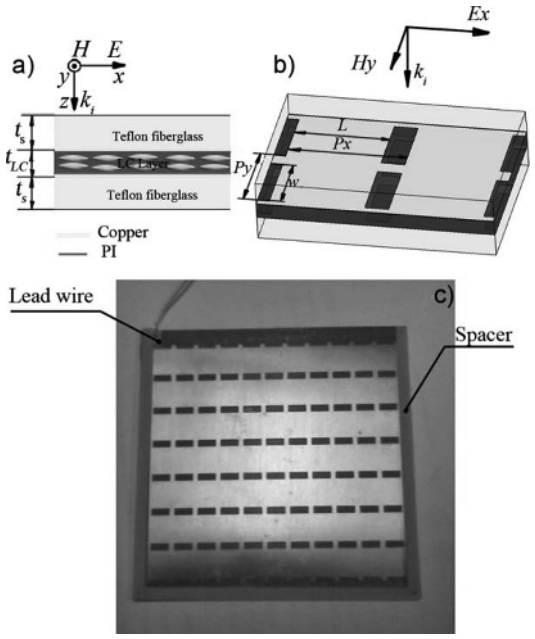

Figure 1.15. *Schematic of the basic cell of a fishnet metamaterial operating at microwave and consisting of two staked rectangular aperture arrays (side view a), 3D view b) and image c)). The top layer was removed for clarity. The metal dielectric stack creates a current loop under normal incidence of the incident wave*

To the best of our knowledge, one of the first experiments, showing that a stack of subwavelength holes arrays may involve left-handed transmission, was conducted at the Spanish Public University of Navarra [BER 05, BER 06, BER 07]. The authors showed that a stack of aluminum plates drilled with subwavelength holes arrays can be compared to a double negative media with backward propagation for a wave normally impinging to the stack. Since this

first article, numerous papers have been published in this field by determining the necessary conditions for designing a negative index material. Notably, it was recognized that a minimum of two layers have to be stacked, a single layer behaving as a conventional frequency selective surface (FSS).

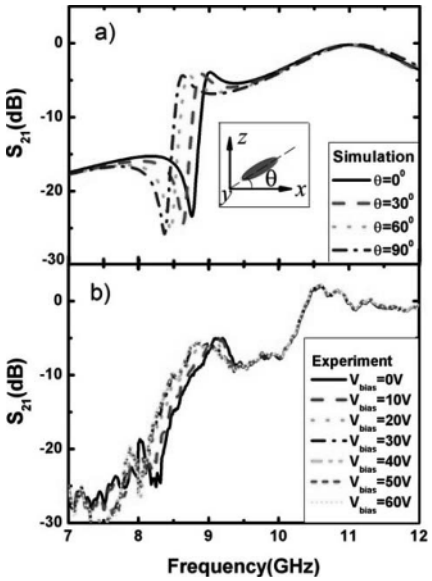

Figure 1.16. *Frequency dependence of the transmission coefficient (calculated a) and measured b)). Tunability of the dispersion characteristics is achieved with liquid crystal technology infiltrated between the two large area parallel metal plates*

In the following, we present another example based on the stacking of subwavelength hole arrays for terahertz frequencies. Figure 1.17 illustrates the various issues that have been solved toward this goal from the point of view of the fabrication and experiments. As exemplified in the first part of this chapter, devoted to the omega-shaped basic cell, the first challenge was to choose a monolithic integration of the structures, whereas manual assembling of individual drilled aluminum plates was performed in the aforementioned works. For this terahertz design, submicron gold films embedded in BCB dielectric layers have been used. In addition, in order to avoid the influence of the GaAs substrate, a membrane-like structure was fabricated in the last stage. For the cell design, full wave analysis shows that an elliptical-shaped aperture with an aspect ratio close to 2:1 allows high transmission levels in the left-handed dispersion branch. These specific features are illustrated in Figure 1.17(a) that depicts (1) the top layer of a

stack with elliptical apertures patterned by optical lithography, (2) the inset of this figure that shows an image of the free-standing array fabricated by deep selective chemical etching and (3) an SEM of the cross-section of a stack of four metal films (their thickness is typically 0.4 μm for a BCB layer of thickness around 30 μm). These devices were subsequently characterized by TDS, which the pump-probe scheme outlined in the previous section. The typical frequency dependences of the magnitude and the phase of the transmission are displayed in Figure 1.18.

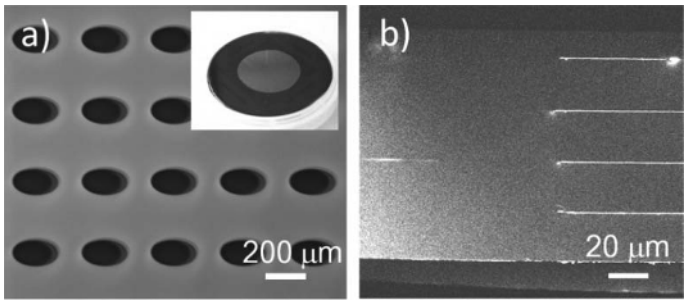

Figure 1.17. *a) Image of a membrane fishnet-like prototype fabricated by stacking subwavelength hole arrays with elliptical-shaped apertures, image of the 2 inch wafer in inset. b) Scanning electron micrograph of the 0.4 μm thick metal/26 μm thick dielectric stacking*

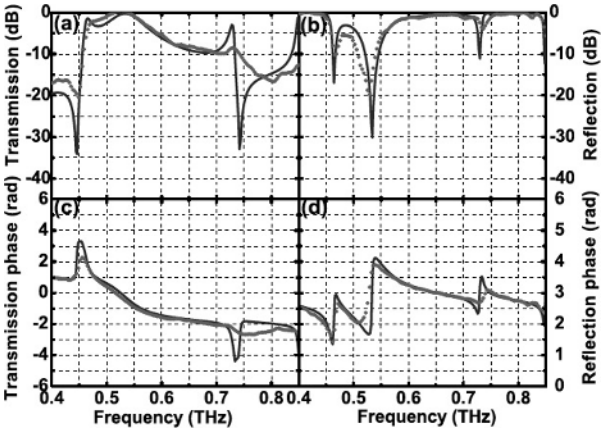

Figure 1.18. *Comparison of the scattering parameters measured by time domain spectroscopy (shadow symbols) and calculated using HFSS ™ (black line) of stacked subwavelength hole metal layers operating at terahertz frequencies. Propagation is backward (phase advance) for the first transmission peak*

The retrieval of the effective permittivity and permeability parameters confirms that the first peak in the transmission, at about 450 GHz, corresponds to negative index values. In contrast, the second peak can be attributed to a right-handed dispersion branch located at higher frequencies. These conclusions are corroborated by full wave analysis [CRO 09] and by lumped element approaches [CAR 10]. In addition, a parametric study as a function of the number of layers first confirms that the canonical structure for negative index must integrate at least two metal layers and also illustrates the possibility of achieving a balanced CRLH regime [WAN 10a]. Comparing the transmission spectra of fishnet structures and subwavelength hole arrays shows similar trends. In fact, both structures operate on the same basic principle, notably artificial magnetism via the creation of a current loop between adjacent metal layers.

In the previous section, we have considered a slab made up of hole arrays. In this case, the demonstration of negative index regime is not direct and uses Fresnel relation inversion techniques. How can we directly assess that such a structure refracts negatively? The most straightforward experiment is a measurement of the refracted angle for a wedge-type device. This is considered in the following.

1.4.3. *Wedge-type devices*

Figure 1.19 illustrates the set-up used toward this goal [WAN 10b]. It is based on angle-resolved measurement of the transmitted beam through a wedge-type device. In practice, the device was monolithically integrated using the technological process described in the previous section (0.3 μm gold films between 26 μm BCB interlayers). The main difference arises from the step-like structure for implementing the slanting side of the prism (see Figure 1.20).

Unlike the measurement of the complex scattering parameters (magnitude and phase of S_{ij}), only the magnitude of the transmission was measured at various angles. This analysis is similar to the one performed in the study of the refraction properties by omega chain arrays. Indeed, the refracted angle is deduced from the Snell–Descartes law by keeping a normal incidence on the first interface. The time domain variations of the transmitted signal are recorded for each detector rotation. Then, by Fourier transform, it is possible to deduce the frequency dependence of the transmitted beam. The application of this experimental procedure gives the results displayed in Figure 1.20. The measured frequency dependence of the effective index was compared to the values deduced from the radiation pattern in the far field and retrieved numerically from a slab structure.

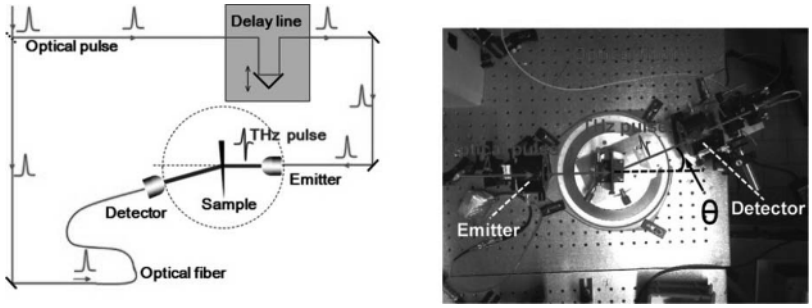

Figure 1.19. *a) Schematic of the angle-resolved TDS set-up (goniometric configuration) aimed at experimentally determining the effective refractive index from the Snell–Descartes law. b) Image of the experimental set-up of the University of Savoy*

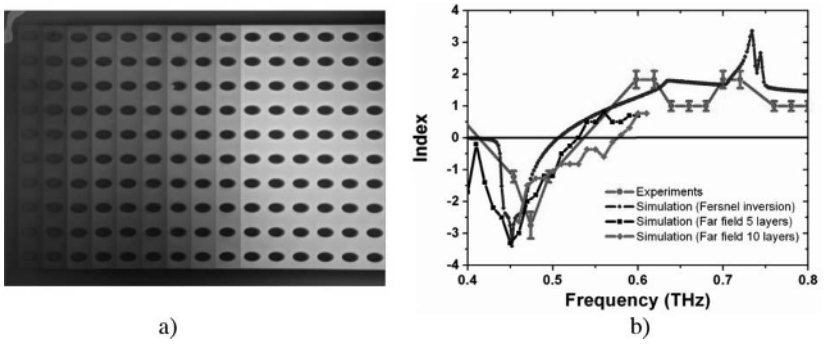

Figure 1.20. *a) Image of a wedge-type metamaterial fabricated by stacking subwavelength hole arrays in a step like prism configuration. b) Frequency dependence of the refractive index measured by using a goniometer and retrieved from the so-called Fresnel inversion technique and by using far-field numerical simulations*

The main goal of the studies presented so far is the control of the dispersion. This means the possibility of switching the operation conditions between left- and right-handed regimes by shifting the operation frequency or tuning by means of ferroelectrics or LC technologies. Are there some novel possibilities afforded by metamaterials to control the polarization of waves and not solely the phase and magnitude? Such prospects have been proposed quite recently with the emergence of chiral metamaterials. In the following, we consider a chiral metamaterial designed from a fishnet arrangement.

1.4.4. *Fishnet with twisted apertures: chiral device*

Chiral devices for achieving double negative media have received widespread attention [PEN 04, PLU 07, TRE 03, PLU 09]. Figure 1.21 shows an image of a prototype aimed at operating at approximately 500 GHz [WAN 13]. The main difference with respect to the previous array of holes is the twisted aperture structure. This topology allows the rotation of the electric field. In fact, the use of an elliptical-shaped aperture, introduced to optimize the level of transmission, involves a sensitivity of the device to the polarization of the electric field. Therefore, it can be shown that the highest transmission level is achieved for an electric field polarized along the small axis of the ellipse. As a consequence, by rotating step-by-step the orientation of the elliptical aperture, we can think that the electric field direction will similarly rotate its orientation. For experimental assessment of this concept, a three-layer prototype is presented. Further details about the TDS experimental method, developed in order to measure the rotary power, can be found in [WAN 13]. In the present experiment, the intensity of the transmitted level is analyzed as a function of the angle between the incident and transmitted beam by a polarized detector. This detector is a dipole antenna integrated with a polarizer on the same rotating stage. From this experimental protocol, we can get the rotation angle θ, which is directly related to the chirality factor, and the ellipticity angle η. For the present device, the orientation of the elliptical aperture has been twisted a 45° step along the three-layered structures. Starting from $\theta = 0$, we thus obtained a rotation of 90° for the last metal plane.

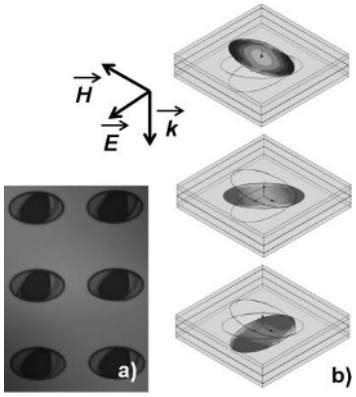

Figure 1.21. *a) Image of a three-layer chiral metamaterial operating at 0.5 THz. A rotary power of 1,000° per wavelength is achieved by twisting the elliptical aperture of a subwavelength hole array prototype by 45° during the stacking. b) Illustration of the rotation of the polarization direction by field mapping at the various metal plates*

The analysis of the different intensity of the transmitted beam as a function of frequency gives the frequency dependence of the rotation angle displayed in Figure 1.22(a). We can note that a rotation magnitude of 90° can be achieved over a distance corresponding to the total thickness of the stack. We can then deduce that the rotary power is as high as 1,000° per wavelength and hence much more efficient than conventional polarization rotators. The other key characteristic is the ellipticity that describes the difference in the attenuation between the right and left circularly polarized waves, denoted as RCP and LCP, respectively. The difference in the attenuation figures for LCP and RCP leads to a deformation of the transmitted beam.

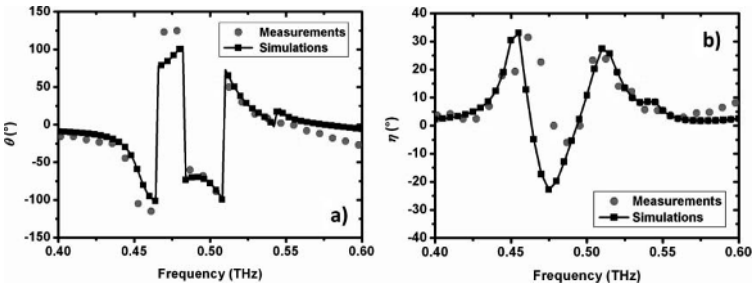

Figure 1.22. *Frequency dependence of the azimuthal rotation a) and of the ellipticity b) angles measured by TDS*

Many features of the propagation of electromagnetic waves are now mastered through the engineering of metal/dielectric artificial material structures on a subwavelength scale. Made up of planar or stratified media, the devices are, however, highly anisotropic as exemplified by the omega-type structures from which the diagonal elements of the permittivity and permeability tensors have been retrieved. The basic concepts, in particular for artificial magnetism, are theoretically irrelevant to the frequency range in which the device operates, but the constitutive elements and more precisely the metal layers are highly dispersive. In the following, we will show that a full dielectric approach also permits us to target artificial magnetism in order to synthesize negative index media.

1.5. Full dielectric approach: Mie resonance-based devices

Most of the concepts used in this section are drawn from the review article published in the journal *Material Today* [ZHA 09b]. We will mainly show here how a magnetic moment can be induced in a dielectric layer. In

addition, we will define the conditions for satisfying the long wavelength regime, which means that the wavelength of the incident wave is much larger than the relevant dimensions used for dielectric structuring.

Basically, the underlying principle for negative permeability values is similar to the aforementioned principle, i.e. an out-of-phase component of the induced field B with respect to the H-field excitation owing to resonance effects originally described by Mie [MIE 08]. By using high-permittivity (κ) dielectrics, two important conclusions can be drawn. First, high displacement current (J_d) can be achieved ($J_d = \varepsilon.\partial E/\partial t$) and the scale over which the resonance takes place is dramatically decreased, owing to the reduction of the wavelength in this high-permittivity media. To sum up, Mie resonance-type devices are generally made up of high κ ferroelectrics cubes or spheres thus with a high degree of symmetry, so that isotropic characteristics can be expected.

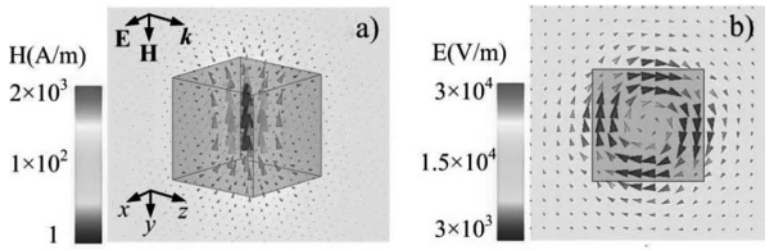

Figure 1.23. *Basic principle of a full dielectric approach by using high permittivity (ferroelectrics BST-cubes). The incident H-field induces a strong circular displacement at the resonance frequency (ground magnetic Mie resonance with an out-of-phase inductive response (B = –1 ⁄μ ⁄ H) above the resonance)*

In order to check these assumptions, Figure 1.24 gives the frequency dependence of the effective permeability for barium strontium titanate (BST) ($BaSrTiO_3$) cubes, with dimensions on a millimeter scale. From the electric field mapping shown in Figure 1.23, it can be checked that a displacement current loop is induced within the cube. This displacement current is responsible for an induced magnetic moment.

The retrieval of the effective permeability by Fresnel inversion, via the calculation of the reflection and transmission coefficients, shows a Lorentz-like dispersion profile with negative values of the permeability μ_{eff} above the resonance frequency. The electric response characterized by the effective permittivity is almost flat. As a result, the BST cube array behaves as a single negative medium (MNG).

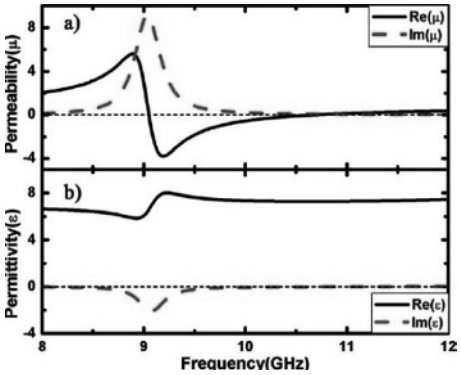

Figure 1.24. *Frequency dependence of μ_{eff} for a high-permittivity cube array. μ_{eff} obeys a Lorentz-type dispersion characteristic similar to the one exhibited by SRR patterns*

The strength of the resonance will depend on the loss tangent (tan $\delta = \varepsilon''/\varepsilon'$ for a complex permittivity $\varepsilon^* = \varepsilon' - j\varepsilon''$). At microwaves, ferroelectric cubes exhibit a typical loss tangent of 1%. In contrast, increasing the operating frequency up to 100 GHz notably degrades the value of $\tan\delta$ up to 10%. There is another drawback in the use of ferroelectric particles, which can be understood from Figure 1.24 in the sense that there is no significant electrical activity at the magnetic resonant frequency. Nevertheless, an electrical Mie resonance exists at higher frequencies. Therefore, more complex structures have to be designed, targeting the achievement of a double negative media and notably those making use of a dual-size super-cell in order to simultaneously fit the magnetic and electric Mie resonances of the cube.

1.5.1. *BST cube technology*

Experimentally, the insensitivity to the incidence can be evidenced with the help of a scattering chamber made up of a parallel plate wave guide whose set-up is illustrated in Figure 1.25 along with an image of the cube arrays characterized for the transverse electric (TE) and transverse magnetic (TM) polarizations. The corresponding measurements are given in the two bottom panels of the right-hand side figure while the results of the calculations by full wave are displayed above.

The first dip in the transmission characteristics, recorded for both TE and TM polarizations, corresponds to the ground magnetic Mie resonance. The insensitivity to the polarization and to the incidence angle is verified.

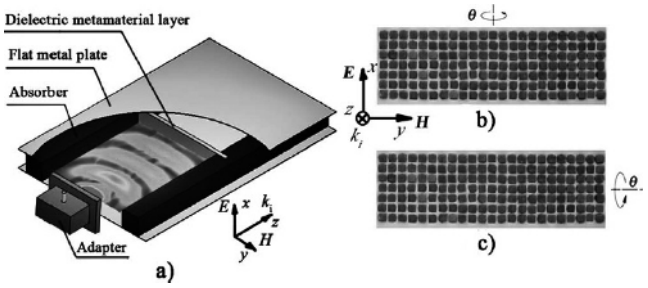

Figure 1.25. *Experimental assessment of artificial magnetism of high-permittivity basic cell (ferroelectrics BST cube with a relative real permittivity of 200). a) Schematic of a scattering chamber with two parallel plates and feeding of the electromagnetic energy via a coaxial to wave guide adapter. b) and c) Image of the ferroelectric cube array for the TE and TM polarization conditions*

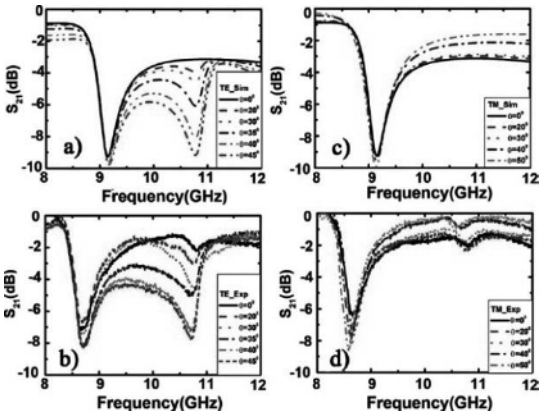

Figure 1.26. *Experimental verification of the isotropy of the dispersion characteristics via full wave analysis (upper panel), by means of incidence field angle scattering parameters measurements (bottom panel)*

1.6. Photonic crystal technology

For telecommunications wavelengths, approximately 1.55 μm, implementing metal-based (plasmonics) metamaterials becomes troublesome owing notably to the high loss level and to the technological difficulties. These conclusions have motivated the search for a full dielectric route.

Among the various possibilities, photonic crystals [LOU 06] based on semiconductor technologies have become very popular and have been widely used for all-angle negative refraction [PER 05, FAB 06].

1.6.1. *Principle*

The underlying concept can be understood from Figure 1.27 showing the band structure calculated for a two-dimensional photonic crystal.

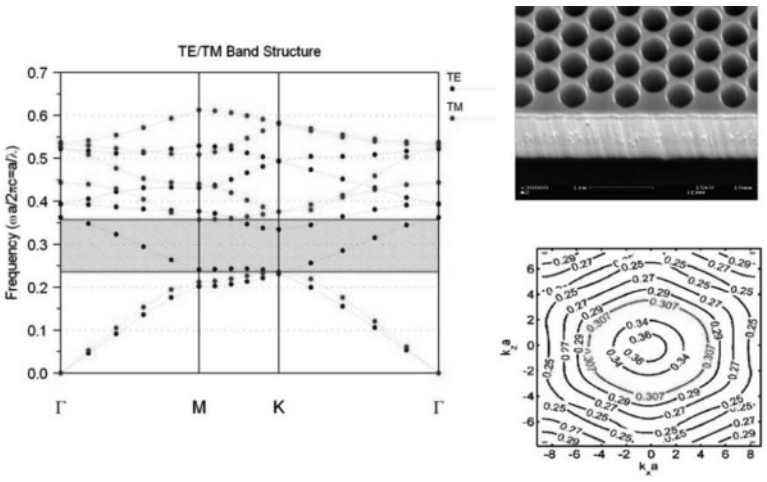

Figure 1.27. *Illustration of the basic principle for negative refraction in photonic crystal microstructures: dispersion diagram in the main symmetry axis of a hexagonal-shaped hole array in a GaAs semiconductor substrate (SEM in inset) for the TE (E perpendicular to the hole axis (y)) and TM mode (E parallel to the y direction). For a TE mode, a second band with a negative curvature (negative index value) is calculated for a reduced frequency between 0.24 and 0.36. The light (ω = c.k) cone where c is the light velocity and k is the wave-vector is crossing this upper-frequency lying dispersion branch around a reduced frequency of 0.3. For this value, the iso-frequency characteristic in the transverse direction k_x and k_z (displayed on the right hand side) is round shaped. All angle refraction can be envisaged for this operating frequency with an effective index n= –1*

This structure consists of a hole array etched in a semiconductor slab. The eigenstates are shown for the high-symmetry directions and for the two polarizations TE and TM, depending on the orientation of the electric and magnetic fields with respect to the hole axis. This band structure shows, in particular, the possibility of propagating TE backward waves in the frequency band between the reduced frequencies 0.24 and 0.36 (shaded region). Indeed,

in this frequency band, we can note that group velocity (v_g) defined as the derivative of the angular frequency (ω) relative to the k vector $v_g = \partial\omega/\partial k$ and the phase velocity $v_p = \omega/k$ are of opposite signs. The iso-frequencies (see Figure 1.27) show round-shaped contours around 0.3 (reduced frequency), which correspond to an effective refractive index equal to –1. Under this condition, it can be expected that the effective value of the refractive index will not depend on the k vector.

1.6.2. *Flat lens*

The fact of having an isotropic value of the effective refractive index permits us to envisage the fabrication and subsequent experimental verification of the so-called Veselago lens [FAB 08, SCH 10]. Let us recall that Veselago first proposed the idea of focusing a point source by means of a flat lens in 1968. The principle of such a focusing can be easily understood with the ray tracing superimposed on the scanning electron microphotograph (SEM) of a photonic crystal (PC) flat lens integrating hole arrays as previously discussed (see Figure 1.29). The light radiated from a ridge optical wave guide in front of the lens refracts negatively at the first and second interfaces with the air embedding medium. A virtual focus within the lens and the formation of an image spot at the back of the lens result from this double negative refraction effect. The frequency operation is chosen according to $n_{eff} = -1$ as discussed earlier, whatever the incidence angle of the ray impinging onto the various interfaces. Under these conditions, the refracted beams converge within and outside the lens. The resolution is mainly determined by the structuring dimensions. Strictly speaking, the condition of deep subwavelength sizing is not fully encountered in the case of PC since the diameter of the holes and period of the array are 347 and 470 nm, respectively, for a wavelength of 1,550 nm. The ability to focus the light radiated from the optical wave guide with a subwavelength resolution was assessed experimentally by SNOM. Without interface engineering, the transfer of light onto the image spot is relatively poor owing to a strong mismatch at the interface. It is worth mentioning that the matching of the index value $n = 1$ for the embedding medium and $n_{eff} = -1$ for the flat lens is non-sufficient for satisfying impedance matching condition. The reduced impedance defined by $z = (\mu_r/\varepsilon_r)^{1/2}$ is not equal to unity like the modulus of $n = (\mu_r.\varepsilon_r)^{1/2}$ that is equal to 1. It can be shown that a dramatic improvement of the transmissivity can be achieved by implementing an anti-reflection coating (ARC) on the two interfaces with air in front of and behind the lens [SCH 10]. Figure 1.29 illustrates the focusing effect by using a flat PC lens via the mapping of the fields

calculated by full wave analysis and displays the image recorded by SNOM experiments. The experimental verification confirms the success of light transfer into the image with a resolution comparable to the Rayleigh limit after the de-convolution of the influence of the tip probe. This limitation is explained by the use of PC technology rather than a true metamaterial technology for which super-resolution could be expected. Experimentally, two differences with the simulation assumptions have to be taken into account. For guiding the wave into a plane inside the lens, it is necessary to develop, by molecular epitaxy, a three-layered InP/InGaAsP/InP confining structure. Numerically, we thus assume an effective medium index value of 3.26 (average of 3.36 for InGaAsP and 3.16 for InP at the thickness pro rata).

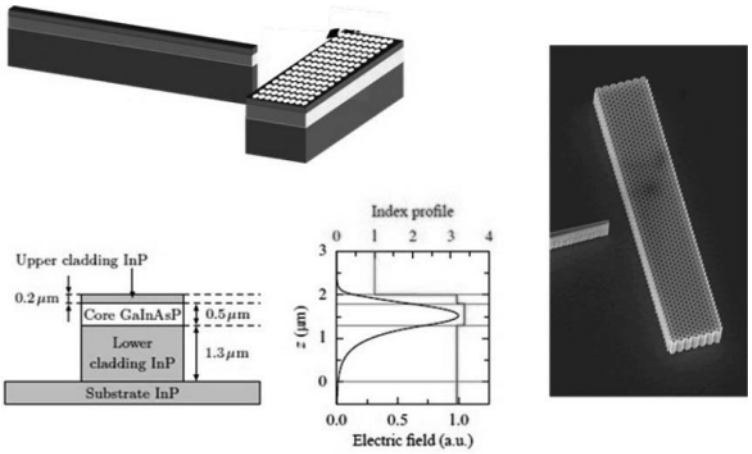

Figure 1.28. *Illustrations of focusing by means of the so-called Veselago flat lens (photonic crystal PC technology) with (1) a schematic of the PC-based device integrating a flat lens and a ridge optical waveguide, (2) a scanning electron micrograph of a prototype that consists of arrayed (hexagonal lattice) holes etched in a three-layered InP/InGaAsP/InP semiconductor hetero-structure and (3) a field mapping in a cross-section*

For an extended control of electromagnetic waves, numerous ideas have recently been proposed on the basis of transformation optics. A survey of these various ideas is beyond the scope of this chapter and the readers will find several examples of transformation optics-based devices in Chapters 6 and 7. However, with a main emphasis on photonic crystal technology applied to dispersion control, it seems interesting to consider the so-called carpet cloaking scheme, also called the ground carpet cloak, as another example.

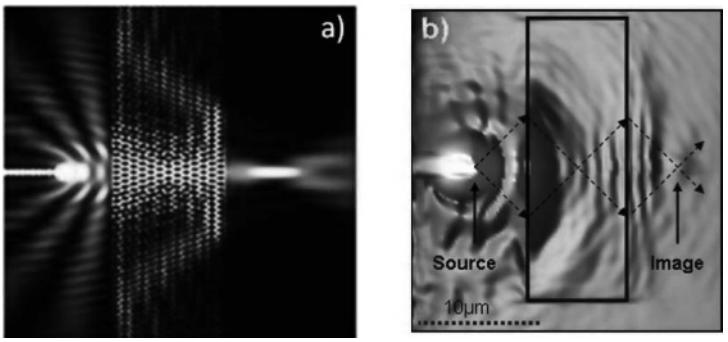

Figure 1.29. *a) Illustration of focusing by using an n = –1 flat lens with a field mapping calculated by FDTD (Rsoft code ™), showing double focusing within and out of the lens after double negative refraction. b) Experimental evidence by scanning near-field optical microscopy (SNOM) imaging. A ray tracing was superimposed onto the SNOM image for illustrating the basic principle of focusing in a negative index medium first proposed by Veselago*

1.6.3. *Carpet cloaking devices*

Basically, a carpet cloak is a reflecting device [LI 08, VAL 09]. In a full cloak [GAI 08], beyond the reconstruction of the phase front of the incident wave in front and behind a potential scatterer, the main goal is to avoid any reflection that could induce standing waves. In contrast, in a carpet cloak, the invisibility device gives the illusion that the scatter does not exist while it is physically placed onto a plane reflecting surface. For illustration of this stealth principle, we consider in the following the case of a carpet cloak fabricated using a photonic crystal technology. By using SNOM measurements, we show that a bump of trapezoidal shape onto a photonic crystal reflecting surface can be invisible with respect to a plane wave impinging onto this irregular surface. Several demonstrations of this invisibility principle use a metallic mirror and a cloak structure made up of PCs.

For the results reported below, the whole set-up is made up of dielectric. In other words, the mirror is made up of a PC semiconductor slab operating in the band gap (hole array). The carpet, which includes an index gradient in order to manipulate the phase front, is fabricated from pillar arrays. The last component of this carpet-on chip device is the integration of an enlarged wave guide, which serves for quasi-plane wave excitation. Figure 1.30 illustrates the design of the cloak via transformation optics techniques and we give a schematic of the SNOM experiment with arrows that depict the

impinging waves. The positions of the pillars, defining the cloak, are set at the nodes of an optical space transformation illustrated in Figure 1.30. Their unequal spacing is used for compensating the phase difference between the incident wave reflected (1) on the top of the trapezoidal-shaped bump, (2) by the slanted interfaces on each side of the bump and (3) the flat back-side interfaces.

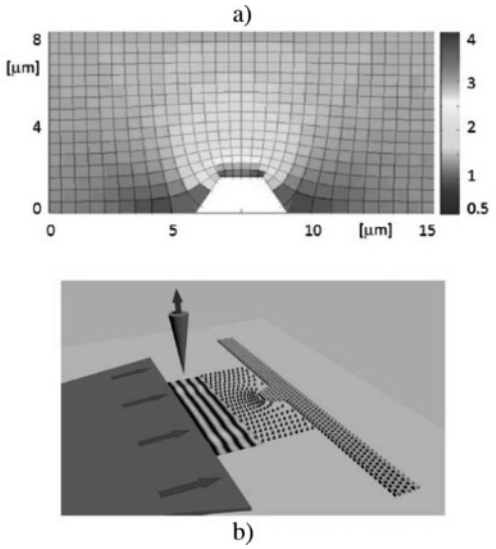

Figure 1.30. *a) Illustration of optical transformation techniques used for a ground carpet invisibility cloak. b) Schematic of the SNOM experiment for assessing plane wave reconstruction in front of a trapezoidal-shaped PC mirror*

Figure 1.31 illustrates the semiconductor-based technologies used to fabricate the mirror PC with a hole array (let us mention that we are using here the band gap regime in a TM mode (see the band structure in Figure 1.25). Figure 1.31 also shows a zoomed view of the cloak fabricated in a single-mask and single-etching stages by the induced coupled plasma (ICP) technique. For verifying the efficiency of such a cloaking scheme under normal incidence, a comparison between a flat mirror, a bare bumped surface and a device dressed with a carpet cloak is displayed in Figure 1.32, which shows topographical images and the optical near-field intensity images recorded by SNOM. From this comparison, it can be noted that the phase fronts are almost flat for the device dressed with a carpet cloak, similarly to a flat reflected surface, whereas some scatterings can be evidenced in the standing wave pattern displayed in the central column.

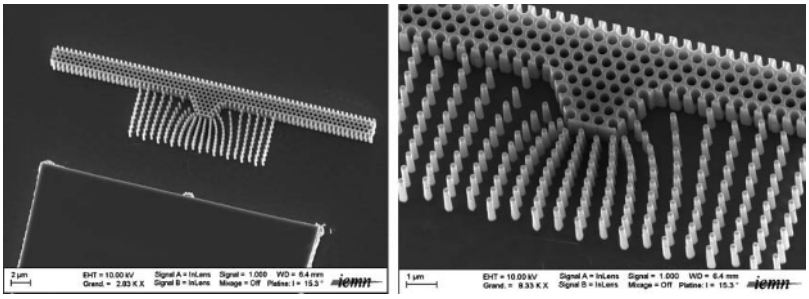

Figure 1.31. *Scanning electron microphotograph of a device operating at telecommunications wavelengths (mid-infrared λ~1.55μm). Illumination of the structure is achieved via a trumpet-shaped ridge wave guide apparent on the top of the left-hand side image. A hole array photonic crystal was designed to operate as a mirror at the wavelength of interest. A pillar array, designed from optical transformations, is integrated in front of a trapezoidal mirror-like scatterer*

1.7. Conclusion and prospects

The possibilities for spatially manipulating the phase fronts and engineering the material dispersion afforded by artificial materials (metamaterials and photonics crystals) have been extended to great extent. In this chapter, it has been shown that several configurations can be chosen as a function of the targeted applications with a clear distinction between a full dielectric approach (high κ Mie resonance media and PCs), which exhibits isotropic properties, and the plasmonic approach resulting in highly anisotropic effective parameters. Beyond the possibility of scaling, at different frequencies, the general basic concepts with the prospect of covering a frequency band from microwave to visible optics, it appears that the dispersion of the constitutive materials gives some frequency limitations. Moreover, and as a general rule, strong dispersion effects require the use of resonance enhancement. As a consequence, the second important limitation is narrow bandwidth related to sharp resonance effects. In addition, this resonance effect increases dramatically the losses in the vicinity of the resonance frequencies. This point is detailed in Chapter 5. What could be the future stages in the development of metamaterial technology?

With respect to the material issue, we can envisage the development of graphene and superconductors with expected cutoff frequencies in the terahertz domain.

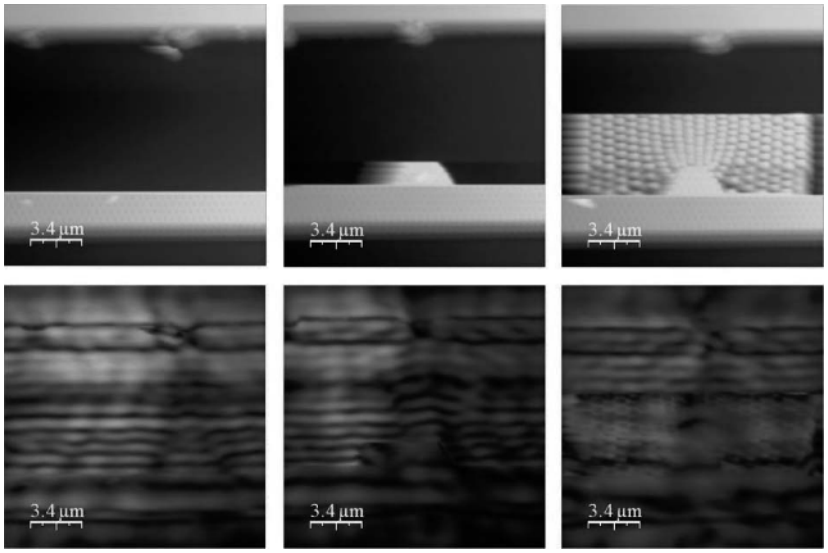

Figure 1.32. *Experimental verification of a mirage effect. The non-flat PC mirror appears as a flat mirror owing to the reflected wave control via the invisibility cloak. For comparison, SNOM imaging of a perfect flat photonic crystal and of a bare scattering surface is also shown in the first and central columns*

From the concept side, quantum metamaterials, which combine electronic confinement in quantum wells and the singular electromagnetic properties of metamaterials, should involve considerable development in the future with a convergence of nanoelectronics and nanophotonics quantum size effects.

Also the so-called hyperbolic metamaterials are considered as a promising route toward a better dispersion control.

From the application side, the number of potentialities is numerous and the main requirement is to overcome the intrinsic losses.

1.8. Acknowledgments

D. Lippens would like to thank all the permanent staff of the DOME group along with the PhD students and post-docs for their contribution to this chapter: L. Burgnies, A.L. Borja, C. Croënne, N. Fabre, M. Hoffman, G. Houzet, L. Kang, É. Lheurette, X. Mélique, V. Sadaune, O. Vanbésien, S. Wang, F. Zhang, J.F. Lampin and X. Wallart of the THz photonics and

Epitaxy groups at IEMN. Special thanks go to J.- L. Coutaz and F. Garet from the University of Savoy, J. Carbonell from the Polytechnic University of Valencia (Spain) , B. Gralak and S. Guenneau from the Fresnel Institute in Marseille (France), F. de Fornel and B. Cluzel from the University of Burgundy in Dijon (France).

1.9. Bibliography

[BER 05] BERUETE M., SOROLLA M., CAMPILLO I., *et al.*, "Enhanced millimeter wave transmission through quasioptical subwavelength perforated plates", *IEEE Transactions on Antennas and Propagation*, vol. 53, pp. 1897–1903, 2005.

[BER 06] BERUETE M., SOROLLA M., CAMPILLO I., "Left-handed extraordinary optical transmission through a photonic crystal of subwavelength hole arrays", *Optics Express*, vol.14, pp. 5445–5455, 2006.

[BER 07] BERUETE M., SOROLLA M., NAVARRO-CIA M., *et al.*, "Extraordinary transmission and left-handed propagation in miniaturized stacks of doubly periodic subwavelength hole arrays", *Optics Express*, vol. 15, pp. 1107–1114, 2007.

[CAI 09] CAI W., SHALAEV V., *Optical Metamaterials: Fundamentals and Applications*, Springer, 2009.

[CAL 04] CALOZ C., ITOH T., "Transmission line approach of left-handed (lh) materials and microstrip implementation of an artificial lh transmission line", *IEEE Transactions on Antennas and Propagation*, vol. 52, pp. 1159–1166, 2004.

[CAL 06] CALOZ C., ITOH T., *Electromagnetic Metamaterials: Transmission Line Theory and Microwave Application*, Wiley Interscience, 2006.

[CAR 10] CARBONELL J., CROENNE C., GARET F., *et al.*, "Lumped elements circuit of terahertz fishnet-like arrays with composite dispersion", *Journal of Applied Physics*, vol. 108, pp. 014907–014913, 2010.

[CRÉ 05] CRÉPIN T., LAMPIN J.-F., DECOOPMAN T., *et al.*, "Experimental evidence of backward waves on terahertz left-handed transmission lines", *Applied Physics Letters*, vol. 87, pp. 104105–104108, 2005.

[CRO 08a] CROENNE C., FOULON M.F., LHEURETTE É., *et al.*, "Negative index metamaterial at 100 GHz", *Proceedings of the European Microwave Association*, vol. 4, pp. 95–101, 2008.

[CRO 08b] CROENNE C., FABRE N., GAILLOT D.P., *et al.*, "Bloch impedance in negative index photonic crystals", *Physical Review B*, vol. 77, pp. 125333–125339, 2008.

[CRO 09] CROENNE C., GARET F., LHEURETTE É., *et al.*, "Left handed dispersion of a stack of subwavelength hole metal arrays at terahertz frequencies", *Applied Physics Letters*, vol. 94, pp. 133112–133115, 2009.

[EBB 98] EBBESSEN T., LEZEC H.J., GHAEMI H.F., *et al.*, "Extraordinary optical transmission through sub-wavelength hole arrays", *Nature*, vol. 391, pp. 667–669, 1998.

[ELE 05] ELEFTHERIADES G.W., BALMAIN K.G., *Negative-refraction Metamaterials: Fundamentals Principles and Applications*, Wiley Interscience, 2005.

[FAB 06] FABRE N., FASQUEL S., LEGRAND C., *et al.*, "Towards focusing using photonic crystal flat lens", *Opto-Electronics Review*, vol. 14, pp. 225–232, 2006.

[FAB 08] FABRE N., LALOUAT L., CLUZEL B., *et al.*, "Optical near-field microscopy of light focusing through a photonic crystal flat lens", *Physical Review Letters*, vol. 101, pp. 073901–073904, 2008.

[GAI 08] GAILLOT D.P., CROENNE C., ZHANG F., *et al.*, "Transformation optics for the full dielectric electromagnetic cloak and metal–dielectric planar hyperlens", *New Journal of Physics*, vol. 10, pp. 115039–115054, 2008.

[GOK 06] GOKKAVAS M., GUVEN K., BULU I., *et al.*, "Experimental demonstration of a left-handed metamaterial operating at 100 GHz", *Physical Review B*, vol. 73, pp. 193103–193107, 2006.

[HUA 04] HUANGFU J., RAN L., CHEN H., *et al.*, "Experimental confirmation of negative refractive index of a metamaterial composed of Omega-like metallic patterns", *Applied Physics Letters*, vol. 84, pp. 1537–1539, 2004.

[JOA 08] JOANNOPOULOS J.D., JOHNSON S.G., WINN J.N., *et al.*, *Photonic Crystals: Molding the Flow of Light*, 2nd ed., Princeton University Press, 2008.

[KAN 11] KANG L., LIPPENS D., "Mie resonance based left-handed metamaterial in the visible frequency range", *Physical Review B*, vol. 83, pp. 195125–195131, 2011.

[LEW 47] LEWIN L., "Electrical constants of a material loaded with spherical particles", *Journal of the Institution of Electrical Engineers*, vol. 94, no. 3, pp. 65–68, 1947.

[LHE 07] LHEURETTE É., VANBÉSIEN O., LIPPENS D., "Double negative media using interconnected omega-type metallic particles", *Microwave and Optical Technology Letters*, vol. 49, pp. 84–90, 2007.

[LI 08] LI J., PENDRY J.B., "Hiding under the carpet: a new strategy for cloaking", *Physical Review Letters*, vol. 101, pp. 203901–203904, 2008.

[LIN 04] LINDEN S., ENKRICH C., WEGENER M., *et al.*, "Magnetic response of metamaterials at 100 terahertz", *Science*, vol. 19, pp. 1351–1353, 2004.

[LIN 06] LINDEN S., ENKRICH C., DOLLING G., WEGENER M., "Photonic metamaterials: magnetism at optical frequencies", *IEEE Journal of Selected Topics in Quantum Electronics*, vol. 12, pp. 1097–1105, 2006.

[LIP 09] LIPPENS D., "Phase-shift, refraction and focusing based on the metamaterial technologies", *Comptes rendus de Physique de l'Académie des Sciences*, vol. 10, no. 5, pp. 400–413, 2009.

[LIU 08] LIU N., GUO H., FU L., *et al.*, "Three-dimensional photonic metamaterials at optical frequencies", *Nature Materials*, vol. 7, pp. 31–37, 2008.

[LIU 09] LIU R., JI C., MOCK J.J., *et al.*, "Broadband ground-plane cloak", *Science*, vol. 323, pp. 366–369, 2009.

[LOU 06] LOURTIOZ J.M., *Photonic Crystals*, Spinger-Verlag, Berlin, Heidelberg, 2006.

[MAR 08] MARQUÉS R., MARTIN F., SOROLLA M., *Metamaterials with Negative Parameters: Theory, Design and Microwave Applications*, Wiley, 2008.

[MAR 09] MARTEAU A., VELU G., HOUZET G., *et al.*, "Ferroelectric tunable balanced right- and left-handed transmission lines", *Applied Physics Letters*, vol. 94, pp. 023507–023510, 2009.

[MIE 08] MIE G., "Beiträge zur optik trüber medien, speziell kolloidaler metallösungen", *Annalen der Physik*, vol. 330, pp. 377–445, 1908.

[OLI 02] OLI A.A., "A periodic structure negative refractive index medium without resonant element", *URSI Digest, IEEE AP-S/URSI International Symposium*, San Antonio, 16–21 June 2002.

[PEN 96] PENDRY J.B., HOLDEN A.J., STEWART W.J., "Extremely low-frequency plasmons in metallic mesostructures", *Physical Review Letters*, vol. 76, pp. 4773–4776, 1996.

[PEN 99] PENDRY J.B., HOLDEN A.J., ROBBINS D.J., *et al.*, "Magnetism from conductors and enhanced nonlinear phenomena", *IEEE Transactions on Microwave Theory and Techniques*, vol. 47, pp. 2075–2084, 1999.

[PEN 04] PENDRY J.B., "A chiral route to negative refraction", *Science*, vol. 306, pp. 1353–1355, 2004.

[PER 05] PERRIN M., FASQUEL S., DECOOPMAN T., *et al.*, "Left-handed electromagnetism obtained via nanostructured metamaterials: comparison with that from microstructured photonic crystals", *Journal of Optics A: Pure and Applied Optics*, vol. 7, p. S3, 2005.

[PLU 07] PLUM E., FEDOTOV V., SCHWANECKE A.S., *et al.*, "Giant optical gyrotropy due to electromagnetic coupling", *Applied Physics Letters*, vol. 90, pp. 223113–223116, 2007.

[PLU 09] PLUM E., ZHOU J., DONG J., *et al.*,"Metamaterial with negative index due to chirality", *Physical Review B*, vol. 79, pp. 035407–035414, 2009.

[RAM 08] RAMAKRISHNA S.A., GRZEGORCZYK T.M., *Physics and Applications of Negative Refractive Index Materials*, SPIE Press, Bellingham, WA, 2008.

[SIM 03] SIMOVSKI C.R., "Plane-wave reflection and transmission by grids of conducting omega-particles and dispersion of omega electromagnetic crystals", *AEU – International Journal of Electronics and Communications*, vol. 57, pp. 358–364, 2003.

[SCH 10] SCHERRER G., HOFMAN M., SMIGAJ W., *et al.*, "Interface engineering for improved light transmittance through photonic crystal flat lenses", *Applied Physics Letters*, vol. 97, pp. 071119–07121, 2010.

[SMI 02] SMITH D.R., SCHULTZ S., MARKOS P., *et al.*, "Determination of effective permittivity and permeability of metamaterials from reflection and transmission coefficients", *Physical Review B*, vol. 65, pp. 195104–195109, 2002.

[SOL 09] SOLYMAR L., SHAMONINA E., *Waves in Metamaterials*, Oxford University Press, 2009.

[SOU 07] SOUKOULIS C.M., LINDEN S., WEGENER M., "Negative refractive index at optical wavelengths", *Science*, vol. 315, pp. 47–49, 2007.

[TRE 03] TRETYAKOV S., NEFEDOV I., SIHVOLA A., *et al.*, "Waves and energy in chiral nihility", *Journal of Electromagnetic Waves and Applications*, vol. 17, pp. 695–706, 2003.

[VAL 09] VALENTINE J., LI J., ZENTGRAF T., *et al.*, "An optical cloak made of dielectric", *Nature Materials*, vol. 8, p. 568, 2009.

[VEL 06] VELU G., BLARY K., BURGNIES L., *et al.*, "A 310 deg;/3.6-dB K-band phaseshifter using paraelectric BST thin films", *IEEE Microwave and Wireless Components Letters*, vol. 16, pp.87–89, 2006.

[WAN 10a] WANG S., GARET F., BLARY K., *et al.*, "Composite left/right-handed stacked hole arrays at submillimeter wavelengths", *Journal of Applied Physics*, vol. 107, pp. 074510–074516, 2010.

[WAN 10b] WANG S., GARET F., BLARY K., LIPPENS D., *et al.*, "Experimental verification of negative refraction for a wedge-type negative index metamaterial operating at terahertz", *Applied Physics Letters*, vol. 97, pp. 181902–181903, 2010.

[WAN 13] WANG S., GARET F. LHEURETTE É. ASTIC M., *et al.*, "Optical activity of twisted fishnet-like subwavelength holes arrays", *Applied Physics Materials*, in press, 2013.

[ZHA 08a] ZHANG F., HOUZET G., LHEURETTE É., *et al.*, "Negative-zero-positive metamaterial with omega-type metal inclusions", *Journal of Applied Physics*, vol. 103, pp. 084312–084320, 2008.

[ZHA 08b] ZHANG F., POTET S., CARBONELL J., *et al.*, "Negative-zero-positive refractive index in a prism-like omega-type metamaterial", *IEEE Transactions on Microwave Theory and Techniques*, vol. 56, pp. 2566–2573, 2008.

[ZHA 08c] ZHANG F., ZHAO Q., KANG L., *et al.*, "Magnetic control of negative permeability metamaterials based on liquid crystals", *Applied Physics Letters*, vol. 92, pp. 193104–193107, 2008.

[ZHA 08d] ZHANG F., ZHAO Q., GAILLOT D.P., *et al.*, "Numerical investigation of metamaterials infiltrated by liquid crystal", *Journal of the Optical Society of America B*, vol. 25, pp. 1920–1925, 2008.

[ZHA 08e] ZHANG F., GAILLOT D.P., CROENNE C., *et al.*, "Low-loss left-handed metamaterials at millimeter waves", *Applied Physics Letters*, vol. 93, pp. 083104–083106, 2008.

[ZHA 09a] ZHANG F., KANG L., QIAN Z., *et al.*, "Magnetically tunable left handed metamaterials by liquid crystal orientation, *Optics Express*, vol. 17, pp. 4360–4366, 2009.

[ZHA 09b] ZHAO Q., ZHOU J., ZHANG F., *et al.*, "Mie resonance-based dielectric metamaterials", *Materials Today*, vol. 12, pp. 60–69, 2009.

[ZHA 11] ZHANG F., ZHANG W., ZHAO Q., *et al.*, "Electrically controllable fishnet metamaterial based on nematic liquid crystal", *Optics Express*, vol. 19, pp. 1553–1568, 2011.